Contribution from the Chemistry Department,
University of Virginia, Charlottesville, Virginia 22901

Polarized Optical Absorption Spectra, Crystal-Field Energy Levels, and Transition Line Strengths of Erbium in Tetragonal $Er(C_2O_4)(C_2O_4H)\cdot 3H_2O$

Karl A. Schoene, Zameer Hasan, John R. Quagliano, and F. S. Richardson*

Received January 8, 1991

Locations of 54 crystal-field levels are reported for Er^{3+} in tetragonal $Er(C_2O_4)(C_2O_4H)\cdot 3H_2O$. These levels span the 12 lowest-energy J-multiplet manifolds of the Er^{3+} $4f^{11}$ electronic configuration, and they were located from single-crystal optical absorption measurements performed over the 6000–27 000-cm^{-1} spectral range. Absorption line-strength and polarization data are reported for all transitions that appear in the low-temperature (15 K) absorption spectra between 15 000 and 25 000 cm^{-1}. These transitions originate from the ground crystal-field level of the $^4I_{15/2}$ (ground) multiplet, and they terminate on crystal-field levels split out of seven different excited multiplets labeled as $^4F_{9/2}$, $^4S_{3/2}$, $^2H_{11/2}$, $^4F_{7/2}$, $^4F_{5/2}$, $^4F_{3/2}$, and $^2G_{9/2}$. The transition line-strength and polarization data show that the Er^{3+} ($4f^{11}$) crystal-field states reflect an Er^{3+} site symmetry lower than the crystallographic C_4 axial symmetry, and this is attributed to the hydrogen atoms of the bioxalate ($C_2O_4H^-$) ligands. The crystal structure of $Er(C_2O_4)(C_2O_4H)\cdot 3H_2O$ exhibits oxalate ↔ bioxalate disorder, and this disorder permits crystallographic C_4 axial symmetry. However, if the Er^{3+} ions are considered individually, each has two oxalate and two bioxalate ligands in its coordination sphere, and the local crystal-field (site) symmetry must be either C_2 or C_1. The ground-state magnetic properties of $Er(C_2O_4)(C_2O_4H)\cdot 3H_2O$ and Er^{3+}-doped $Y(C_2O_4)(C_2O_4H)\cdot 3H_2O$ have been reported previously (see ref 3), and they also indicate nonaxially symmetric contributions to the crystal-field interactions in these systems.

Introduction

The most common coordination polyhedron found among 9-coordinate lanthanide complexes is that of a tricapped trigonal prism.[1] Much less common is the monocapped square antiprism found in tetragonal crystals of $Er(C_2O_4)(C_2O_4H)\cdot 3H_2O$ (where $C_2O_4^{2-}$ and $C_2O_4H^-$ denote oxalate and bioxalate anions, respectively).[2] The coordination environment of the erbium ions in $Er(C_2O_4)(C_2O_4H)\cdot 3H_2O$ is more complex than the stoichiometric formula might suggest, and this complexity is reflected in the optical absorption spectra of the erbium 4f–4f electronic transitions. In this paper, we report transition line strengths and crystal-field energy-level data obtained from optical absorption measurements on single crystals of $Er(C_2O_4)(C_2O_4H)\cdot 3H_2O$, and we relate these spectroscopic results to specific structural features in the erbium coordination environment. Optical studies of $Er(C_2O_4)(C_2O_4H)\cdot 3H_2O$ have not been reported previously in the literature, but O'Conner and Carlin[3] have reported low-temperature (1.5–20 K) magnetic susceptibility results obtained for single crystals of *neat* $Er(C_2O_4)(C_2O_4H)\cdot 3H_2O$ and low-temperature (4.2 K) EPR measurements for Er^{3+} *doped* into $Y(C_2O_4)(C_2O_4H)\cdot 3H_2O$.

Structure Considerations

The compound $Er(C_2O_4)(C_2O_4H)\cdot 3H_2O$ crystallizes in the tetragonal space group $P4/n$ with two formula weights per unit cell.[2] Each Er^{3+} ion is coordinated to two oxalate ($C_2O_4^{2-}$) and two bioxalate ($C_2O_4H^-$) ligands via bidentate chelation, and the resulting ErO_8 coordination cluster has the shape of a distorted square antiprism in which one square face is larger than the other (3.12 Å versus 2.73 Å edge lengths). Each of the four five-membered chelate rings has one oxygen atom at a corner of the larger square face (2.362-Å Er–O distance) and one at a corner of the smaller face (2.418-Å Er–O distance), and together the chelate rings form a four-bladed propeller with either left-handed (Λ) or right-handed (Δ) helicity about the C_4 symmetry axis of the ErO_8 coordination polyhedron (see Figure 1). A water molecule is located on the C_4 symmetry axis and caps the larger square face of this polyhedron. The Er–O(water) distance is 2.441 Å. The ErO_9 coordination cluster (defined to include the water oxygen atom) has *exact* C_4 point-group symmetry, but it deviates only slightly from C_{4v} point-group symmetry. When the chelate rings of the erbium–oxalate (and bioxalate) coordination are taken into consideration, the approximate reflection planes are entirely destroyed, but C_4 symmetry at the Er^{3+} site is retained if the hydrogen atoms of the water and bioxalate ligands are disregarded. If these hydrogen atoms are considered, the site symmetry at Er^{3+} cannot be higher than C_2. The crystal structure of $Er(C_2O_4)(C_2O_4H)\cdot 3H_2O$ exhibits oxalate ↔ bioxalate disorder, and X-ray diffraction data cannot be used to assign the stoichiometric bioxalate hydrogen atoms to specific ligands in the coordination sphere of any given Er^{3+} ion.[2]

Each of the $C_2O_4^{2-}$ and $C_2O_4H^-$ ligands coordinated to a given Er^{3+} ion in the $Er(C_2O_4)(C_2O_4H)\cdot 3H_2O$ crystal structure is also coordinated (via bidentate chelation) to a second Er^{3+} ion. Therefore, each Er^{3+} ion in a given *ab* plane of the crystal is "bridged" to four other Er^{3+} ions located in the same crystallographic plane. All of the erbium coordination spheres are structurally identical *except* with respect to the helical screw sense of their chelate-ring arrangement (the four-bladed propeller) about the C_4 symmetry axis of the coordination polyhedron. The chelate-ring arrangements around adjacent Er^{3+} ions (that share a common ligand) must have helicities of *opposite handedness*. Each Er^{3+} ion in the crystal has a *chiral* coordination environment, but the coordination environments associated with each *pair* of adjacent Er^{3+} ions represent a racemate of enantiomeric structures, and the overall crystal is racemic.

The magnetic susceptibility data reported by O'Conner and Carlin[3] (for single crystals of neat $Er(C_2O_4)(C_2O_4H)\cdot 3H_2O$) showed Curie–Weiss law behavior over the 1.5–20 K temperature range, and they yielded g values of $g_\parallel = 12.97$ and $g_\perp = 2.98$. The EPR measurements reported by O'Conner and Carlin[3] for Er^{3+}-doped single crystals of $Y(C_2O_4)(C_2O_4H)\cdot 3H_2O$ (at 4.2 K) yielded g values of $g_\parallel = 12.9$, $g_x = 3.38$, and $g_y = 2.41$. The anisotropy in these g values suggests a small deviation from axial symmetry at the Er^{3+} sites, which is possibly attributable to the influence of the bioxalate hydrogen atoms.

Experimental Section

Crystals of $Er(C_2O_4)(C_2O_4H)\cdot 3H_2O$ were grown from slowly evaporating solutions of erbium oxalate in concentrated hydrochloric acid at room temperature.[2,3] The growth rate of crystals suitable for polarized optical absorption measurements is very slow, and the harvest yield of optical-quality crystals is low. The crystals used in our optical studies grew as thin square plates, with the unique (optic) axis of the crystal normal to the square face.

For variable-temperature optical measurements, crystals were attached with indium foil to a one-piece stage (machined from oxygen-free copper), and the stage was bolted to the cold head of a CTI-Cryogenics closed-cycle helium refrigerator/cryostat. The cold-head temperature was varied and controlled (at temperatures between 10 and 300 K) by use of a Lake Shores Cryotronics Model DRC-70 temperature controller. Unpolarized *axial* absorption spectra and σ- and π-polarized *orthoaxial*

* To whom correspondence should be addressed.

(1) Sinha, S. P. *Struct. Bonding* **1976**, *25*, 70.
(2) Steinfink, H.; Brunton, G. D. *Inorg. Chem.* **1970**, *9*, 2112.
(3) O'Conner, C. J.; Carlin, R. L. *Chem. Phys. Lett.* **1977**, *49*, 574.

0020-1669/91/1330-3813$02.50/0

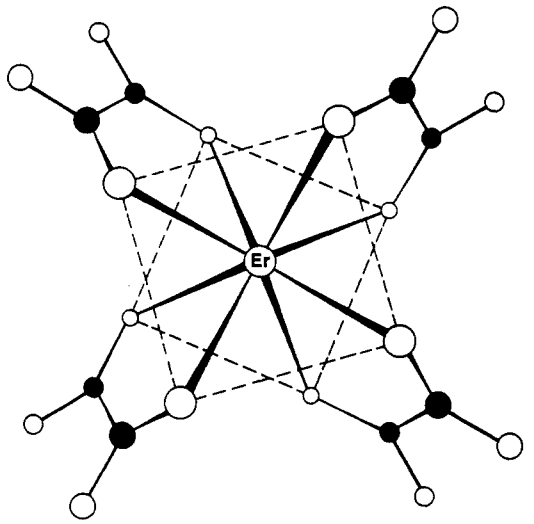

Figure 1. View down the C_4 symmetry axis of an $Er(C_2O_4)_4$ coordination complex in $Er(C_2O_4)(C_2O_4H)\cdot 3H_2O$. This structure has right-handed (Δ) configurational chirality about the Er^{3+} ion. The dashed lines show the square faces of the ErO_8 coordination polyhedron.

absorption spectra were recorded with a Cary Model 2415 UV/vis near-IR spectrophotometer. Axial absorption spectra were measured over the 6000–27 000-cm^{-1} wavenumber range, and orthoaxial absorption measurements were performed over the 15 000–27 000-cm^{-1} wavenumber range.

Optical Selection Rules and Data Analysis

Selection Rules. It was noted in an earlier section of this paper that the coordination environment around each Er^{3+} ion in $Er(C_2O_4)(C_2O_4H)\cdot 3H_2O$ has C_4 point-group symmetry if the bioxalate and water hydrogen atoms are ignored. Therefore, it is reasonable to expect that the energy levels split out of the $4f^{11}$ electronic configuration of Er^{3+} will reflect C_4 crystal-field symmetry and may be classified according to how their eigenstates transform under the symmetry operations of the C_4 double-group (C_4^*). Each energy level is a Kramers doublet, and assuming C_4 crystal-field symmetry, each may be assigned either an E′ or an E″ label (where E′ and E″ denote irreducible representations in the C_4^* double-group). Among the total angular momentum eigenfunctions $|JM_J\rangle$ of the $4f^{11}$ electronic configuration, those with $M_J = {}^1/_2, {}^7/_2, {}^9/_2, {}^{15}/_2$, and ${}^{17}/_2$ transform as E′ in the C_4^* double-group and those with $M_J = {}^3/_2, {}^5/_2, {}^{11}/_2$, and ${}^{13}/_2$ transform as E″.

The (μ_x,μ_y) and (m_x,m_y) Cartesian components of the electric (μ) and magnetic ($\mathbf{m}$) dipole moment operators transform as the E irreducible representation (irrep) in the C_4^* double-group, and the μ_z and m_z components transform as the A irrep. Both the E and A irreps are contained in the E′ × E′ and E″ × E″ direct-product representations of C_4^*, whereas E, but not A, is contained in the E′ × E″ direct-product representation. Therefore, optical transitions between crystal-field levels of identical symmetry (i.e., E′ → E′ or E″ → E″) can exhibit electric and magnetic dipole polarizations both parallel and perpendicular to the C_4 symmetry axis, whereas transitions of the E′ → E″ or E″ → E′ type can only exhibit electric and magnetic dipole polarizations that are perpendicular to the C_4 symmetry axis. Since the local C_4 symmetry axes at the Er^{3+} sites in $Er(C_2O_4)(C_2O_4H)\cdot 3H_2O$ are parallel to the optic axis of the crystal, these selection rules lead directly to the selection rules shown in Table I for single-crystal *axial* and *orthoaxial* optical measurements.

Among the eleven J-multiplet to J-multiplet transition manifolds examined in this study, only one ($^4I_{15/2} \rightarrow {}^4I_{13/2}$) is predicted to have significant magnetic dipole character.[4] Therefore, the selection rules of Table I indicate that comparisons of σ- and π-polarized *orthoaxial* absorption spectra (outside of the $^4I_{15/2} \rightarrow {}^4I_{13/2}$ transition region) should permit clear-cut differentiation

(4) Schoene, K. A. Ph.D. Dissertation, University of Virginia, 1989.

Table I. Electric (μ) and Magnetic (m) Dipole Selection Rules

		orthoaxial spectra	
transition	axial spectra	σ-polarized	π-polarized
E′ → E′	(μ_x,μ_y); (m_x,m_y)	(μ_x,μ_y); m_z	μ_z; (m_x,m_y)
E″ → E″	(μ_x,μ_y); (m_x,m_y)	(μ_x,μ_y); m_z	μ_z; (m_x,m_y)
E″ ↔ E′	(μ_x,μ_y); (m_x,m_y)	(μ_x,μ_y)	(m_x,m_y)

between E″ ↔ E′ versus E″ ↔ E″ (or E′ ↔ E′) crystal-field transitions, *if* the energy-level structure of the Er^{3+} $4f^{11}$ electronic configuration reflects C_4 crystal-field symmetry. If the bioxalate hydrogen atoms in the $Er(C_2O_4)(C_2O_4H)\cdot 3H_2O$ structure reduce the "effective" crystal-field symmetry to C_2 (or C_1), the erstwhile E′ and E″ states will be mixed and the selection rules of Table I will be, at best, approximate. It is unlikely that the bioxalate hydrogen atoms will have significant *direct* interactions with the 4f electrons of the Er^{3+} ions. However, it is highly likely that they will perturb the charge distributions on the oxygen atoms that are coordinated directly to Er^{3+}.

Transition Line Strengths. Intensities of transitions occurring between crystal-field levels are reported here in terms of transition line strengths. Separate line strengths were determined for transitions observed in unpolarized *axial* (α) absorption spectra and in σ- and π-polarized *orthoaxial* absorption spectra. For a transition between levels A (initial) and B (final), the respective line strengths were determined according to the following expressions:

$$S_{AB}(\alpha) = 3.06 \times 10^{-39}[g_A/c_m l X_A(T)] \int_{A\rightarrow B} A_\alpha(\bar{\nu},T)\, d\bar{\nu}/\bar{\nu} \ (\text{esu}^2\text{cm}^2) \quad (1)$$

$$S_{AB}(\text{p}) = 3.06 \times 10^{-39}[g_A/c_m l X_A(T)] \int_{A\rightarrow B} A_\text{p}(\bar{\nu},T)\, d\bar{\nu}/\bar{\nu} \ (\text{esu}^2\ \text{cm}^2) \quad (2)$$

Here p denotes σ or π polarization, g_A is the electronic degeneracy of level A, $X_A(T)$ is the fractional thermal (Boltzmann) population of level A at temperature T, c_m denotes molar concentration (mol/L) of absorbing species (Er^{3+} ions), l denotes sample thickness (in cm), A_α and A_p (p = σ or π) are decadic absorbances measured in the axial and orthoaxial absorption experiments, respectively, and the integrations are over the wavenumber interval spanned by the $A \rightarrow B$ absorption band (with $\bar{\nu}$ expressed in cm^{-1}). For Er^{3+} in $Er(C_2O_4)(C_2O_4H)\cdot 3H_2O$, we have $g_A = 2$ and $c_m(Er^{3+}) = 6.88$ mol/L.[2]

All of the transition line strengths reported in this paper were determined from intensity measurements performed on samples at ~15 K, and all are assigned to transitions that originate from the *ground* crystal-field level of the $^4I_{15/2}$ (ground) multiplet manifold. Transitions from other crystal-field levels of $^4I_{15/2}$ were observed in absorption spectra obtained at higher sample temperatures, but the line strengths of these transitions were not determined.

If we assume that only electric dipole and magnetic dipole transition processes contribute to the observed line intensities, then the line strengths (S_{AB}) defined by eqs 1 and 2 may be expressed as follows:

$$S_{AB}(\alpha) = \chi_\alpha D^e_{AB,1} + \chi_\alpha' D^m_{AB,1} \quad (3)$$

$$S_{AB}(\sigma) = \chi_\sigma D^e_{AB,1} + \chi_\sigma' D^m_{AB,0} \quad (4)$$

$$S_{AB}(\pi) = \chi_\pi D^e_{AB,0} + \chi_\pi' D^m_{AB,1} \quad (5)$$

Here χ and χ' are correction factors for bulk (sample) refractivity effects on the electric dipole and magnetic dipole components of the radiation field, and

$$D^e_{AB,q} = |\sum_a \sum_b \langle Aa|\mu_q|Bb\rangle|^2 \quad (6)$$

$$D^m_{AB,q} = |\sum_a \sum_b \langle Aa|m_q|Bb\rangle|^2 \quad (7)$$

where μ_q and m_q denote components of the electric and magnetic dipole moment operators, expressed in a spherical basis (q = 0,

± 1) in which the $q = 0$ basis vector is defined to be parallel to the 4-fold symmetry axis of the crystal. The summations in expressions (6) and (7) are over the degenerate components of levels *A* and *B*. The selection rules of Table I conform to expressions (3)–(7) *if* the *A* and *B* spectroscopic states are eigenstates of a C_4 crystal-field Hamiltonian (and the C_4 symmetry axis of the crystal-field potential at the Er^{3+} sites is aligned parallel to the crystallographic 4-fold axis).

Energy-Level Calculations. Among the 59 crystal-field levels associated with the 12 lowest energy *J*-multiplets of the Er^{3+} $4f^{11}$ electronic configuration, 54 were located from our spectroscopic measurements. These levels span the 0–27 000-cm^{-1} range. The spectroscopic results showed significant deviations from the selection rules of Table I in several transition regions, and assignments of levels, based on C_4 crystal-field symmetry considerations, were fraught with ambiguities. However, tentative assignments were made for 30 of the levels (i.e., these levels were assigned to either an E′ or E″ irrep of the C_4* double-group), and attempts were made to fit the empirical energy level data with a parametrized model Hamiltonian of C_4 symmetry.

The model Hamiltonian was defined to operate only *within* the $4f^{11}$ electronic configuration of Er^{3+}, and it was partitioned into an *atomic* part ($\hat{H}_a$) and a *crystal-field* part ($\hat{H}_{cf}^+$). The atomic Hamiltonian was defined according to

$$\hat{H}_a = E_{av} + \sum_k F^k\hat{f}_k + \alpha\hat{L}(\hat{L}+1) + \beta\hat{G}(G_2) + \gamma\hat{G}(R_7) + \sum_i T^i\hat{t}_i + \zeta_{so}\hat{A}_{so} + \sum_k P^k\hat{p}_k + \sum_j M^j\hat{m}_j \quad (8)$$

where $k = 2, 4, 6$, $i = 2, 3, 4, 6, 7, 8$, $j = 0, 2, 4$, and the operators (ô) and their associated parameters are written according to conventional notation *and* meaning (with respect to the interactions they represent).[5-7] The crystal-field Hamiltonian was defined according to

$$\hat{H}_{cf}^+ = \sum_{k,m}\sum_i B_{km}\hat{u}_{km}(i) \quad (9)$$

where *i* labels the 4f electrons, $\hat{u}_{km}(i)$ is a one-electron unit-tensor operator, and B_{km} denotes a standard (one-electron) crystal-field interaction parameter. Only the *even-parity* components of the crystal-field interaction potential are contained in $\hat{H}_{cf}^+$, and if the interaction potential is assumed to have C_4 point-group symmetry, the nonvanishing components of the $\hat{H}_{cf}^+$ operator may be chosen as: $(k,m) = (2,0)$, $(4,0)$, *Re* and *Im* $(4,\pm 4)$, $(6,0)$, and *Re* $(6,\pm 4)$, where *Re* and *Im* indicate real and imaginary parts of *complex* operator components.[8]

The atomic Hamiltonian, defined by eq 8, contains 20 parameters (including E_{av}), and the crystal-field Hamiltonian, defined by eq 9 and assuming C_4 symmetry, contains five parameters (one of which has both *real* and *imaginary* parts). The *complete*, $\hat{H}_a + \hat{H}_{cf}^+$, Hamiltonian was used in all of our energy-level calculations, although not all of the 20 parameters contained in $\hat{H}_a$ were treated as free variables in performing parametric fits of calculated-to-experimental energy-level data (vide infra). In all of our energy-level calculations, the total (atomic + crystal-field) Hamiltonian was diagonalized within the *complete* $4f^{11}$ $SLJM_J$ basis set (comprised of 364 states).

We performed a series of additional energy-level calculations in which the crystal-field Hamiltonian was augmented by terms with symmetry *lower* than C_4 (for example, $(k,m) = (2,\pm 2)$, $(4,\pm 2)$, $(6,\pm 2)$, and $(6,\pm 6)$). These calculations yielded improved fits to the empirical energy-level data, but the empirical data sets were too small to permit a definitive parametric analysis based on the augmented crystal-field Hamiltonian. However, these calculations *do* support the view that the 4f-electron/crystal-field interactions in $Er(C_2O_4)(C_2O_4H)\cdot 3H_2O$ contain nonaxially symmetric components that might be attributed to perturbations by the bioxalate hydrogen atoms.[3,4]

Table II. Calculated and Observed Energy Levels for Er^{3+} ($4f^{11}$) in Tetragonal $Er(C_2O_4)(C_2O_4H)\cdot 3H_2O$

level no.	multiplet[a]	energy/cm^{-1} calcd[b]	obsd[c]	Δ[d]
1	$^4I_{15/2}$	4	0	4
2		76	85	−9
3		110	118	−8
4		158		
5		198		
6		281		
7		321		
8		366		
9	$^4I_{13/2}$ (6690)	6600	6605	−5
10		6642	6629	13
11		6666	6657	9
12		6704	6692	12
13		6712	6705	7
14		6761	6752	9
15		6798	6793	5
16	$^4I_{11/2}$ (10319)	10263	10278	−15
17		10285	10291	−6
18		10305	10314	−9
19		10316	10327	−11
20		10333	10339	−6
21		10364	10364	0
22	$^4I_{9/2}$ (12527)	12415	12427	−12
23		12466	12485	−19
24		12519	12518	1
25		12585	12563	22
26		12657	12643	14
27	$^4F_{9/2}$ (15400)	15337	15339	−2
28		15361	15353	8
29		15395	15395	0
30		15443	15447	−4
31		15482	15466	16
32	$^4S_{3/2}$ (18514)	18480	18484	−4
33		18543	18544	−1
34	$^2H_{11/2}$ (19271)	19209	19202	7
35		19234	19233	1
36		19261	19256	5
37		19288	19292	−4
38		19306	19303	3
39		19335	19339	−4
40	$^4F_{7/2}$ (20650)	20566	20571	−5
41		20617	20623	−6
42		20670	20681	−11
43		20708	20725	−17
44	$^4F_{5/2}$ (22301)	22278	22286	−8
45		22301	22296	5
46		22323	22320	3
47	$^4F_{3/2}$ (22646)	22616	22608	8
48		22687	22684	3
49	$^2G_{9/2}$ (24684)	24586	24566	20
50		24627	24615	12
51		24671	24673	−2
52		24742	24769	−27
53		24784	24798	−14
54	$^4G_{11/2}$ (26520)	26448	26436	12
55		26467	26461	6
56		26495	26491	4
57		26538	26537	1
58		26584	26584	0
59		26609	26613	−4

[a] Labeled according to principal *SLJ* parentage. Multiplet baricenter energies (expressed in cm^{-1}) are shown in parentheses. [b] Calculated by using the Hamiltonian parameter values listed in Table IV and assuming C_2 crystal-field symmetry. [c] Locations obtained from 15 K absorption measurements and expressed in *vacuum* wavenumber units (cm^{-1}). Uncertainties in the energy-level locations are ca. ± 4 cm^{-1} (on average). [d] Difference between calculated and observed energies.

Results

The energy levels located from our optical absorption measurements are listed in Table II. These levels span the 12 lowest

(5) Crosswhite, H. M.; Crosswhite, H. *J. Opt. Soc. Am. B* **1984**, *1*, 246.
(6) Carnall, W. T.; Goodman, G. L.; Rajnak, K.; Rana, R. S. *J. Chem. Phys.* **1989**, *90*, 3443.
(7) Schoene, K. A.; Quagliano, J. R.; Richardson, F. S. *Inorg. Chem.*, preceding paper in this issue.
(8) Morrison, C. A.; Leavitt, R. P. In *Handbook on the Physics and Chemistry of Rare Earths*; Gachneidner, K., Eyring, L., Eds.; North-Holland Publishing Co.: Amsterdam, 1982; Vol. 5.
(9) Couture, L.; Rajnak, K. *Chem. Phys.* **1984**, *85*, 315.

Table III. Line Strengths of Absorptive Transitions Originating from the Ground Crystal-Field Level of Er^{3+} in Tetragonal $Er(C_2O_4)(HC_2O_4)\cdot 3H_2O$

excited level[a]			line strengths[b]/10^{-42} esu^2 cm^2			
no.	multiplet	$\bar{\nu}$/cm^{-1}	$S(\alpha)$	$S(\sigma)$	$S(\pi)$	P[c]
27	$^4F_{9/2}$	15339	2.8	2.7	1.7	−0.23
28		15353	2.4	2.7	1.3	−0.35
29		15395	9.8	9.8	5.7	−0.26
30		15447	7.2	7.5	5.8	−0.13
31		15466	5.2	5.5	2.6	−0.36
32	$^4S_{3/2}$	18484	0.9	0.7	0.6	−0.08
33		18544	26.2	24.1	2.6	−0.81
34	$^2H_{11/2}$	19202	2.9	3.1	4.3	0.16
35		19233	5.2	5.2	5.2	0
36		19256	7.1	6.9	1.2	−0.70
37		19292	{27.3}	n.d.	n.d.	<0
38		19303		n.d.	n.d.	>0
39		19339	38.1	38.7	13.4	−0.49
40	$^4F_{7/2}$	20571	4.6	4.5	4.7	0.02
41		20623	12.4	13.4	25.5	0.31
42		20681	2.2	2.5	6.1	0.42
43		20725	22.1	19.9	0.7	−0.93
44	$^4F_{5/2}$	22286	{14.4}	n.d.	n.d.	>0
45		22296		n.d.	n.d.	<0
46		22320	9.4	11.1	40.1	0.57
47	$^4F_{3/2}$	22608	2.3	2.2	1.9	−0.07
48		22684	38.3	31.9	1.9	−0.89
49	$^2G_{9/2}$	24566	0.4	0.4	0.1	−0.60
50		24615	1.1	1.1	0.3	−0.57
51		24673	12.2	11.6	3.9	−0.50
52		24769	1.6	1.5	3.3	0.38
53		24798	0.6	1.1	5.9	0.69

[a] Numbering scheme and multiplet labels correspond to those used in Table II. [b] Line strengths were determined from 15 K absorbance data according to eqs 1 and 2 of the text, and they are expressed in units of 10^{-42} esu^2 cm^2 (1 esu cm = 3.3356×10^{-30} C m = 1×10^{18} D). n.d. ≡ not determined. Uncertainties in the line-strength values are ca. ±0.1 × 10^{-42} esu^2 cm^2 (on average). [c] $P = (S(\pi) - S(\sigma))/(S(\pi) + S(\sigma))$.

Table IV. Hamiltonian Parameters Derived from Energy-Level Analyses of Er^{3+} in $Er(C_2O_4)(C_2O_4H)\cdot 3H_2O$

atomic param[a]	value[b]/cm^{-1}	crystal-field param[c]	value/cm^{-1}	
			C_4[d]	C_2[e]
E_{av}	35763	B_{20}	−633	−607
F^2	99759	B_{40}	307	228
F^4	70738	*Re* B_{44}	416	241
F^6	49486	*Im* B_{44}	604	621
α	18.8	B_{60}	−255	−221
β	−614	*Re* B_{64}	−712	−640
γ	1640	*Re* B_{22}	0	−60
T^2	466	*Im* B_{22}	0	−144
T^3	[34]	*Re* B_{42}	0	122
T^4	[76]	*Im* B_{42}	0	−444
T^6	[−340]	*Re* B_{62}	0	45
T^7	[317]	*Im* B_{62}	0	163
T^8	[393]	*Re* B_{66}	0	−212
ζ_{4f}	2377	*Im* B_{66}	0	−79
M^0	[4.50]			
M^2	[2.52]	N	54[f]	54[f]
M^4	[1.71]	σ	14.6[g]	9.9[g]
P^2	732			
P^4	$0.75P^2$			
P^6	$0.50P^2$			

[a] See eq 8 in the text. [b] Values shown in brackets were held fixed in performing calculated-to-empirical energy-level fits. [c] See eq 9 in the text. Real and imaginary parts of complex parameters are identified by *Re* and *Im*, respectively. [d] Constrained to C_4 crystal-field symmetry. [e] Constrained to C_2 crystal-field symmetry. [f] Number of energy levels included in the parametric data fits. [g] Root-mean-square deviation between calculated and observed energies.

energy J-multiplet manifolds of the Er^{3+} $4f^{11}$ electronic configuration, and they are sufficient for determining the baricenter energies of 11 J-multiplets (see the second column of Table II).

Absorption line-strength data are given in Table III for all transitions that appear in the low-temperature (15 K) absorption spectra between 15000 and 25000 cm^{-1}. All of these transitions originate from the ground crystal-field level of the $^4I_{15/2}$ multiplet, and each is expected to occur via a predominantly electric dipole mechanism. If we assume C_4 crystal-field symmetry and apply the electric dipole selection rules of Table I, transitions of symmetry type E′ → E′ *or* E″ → E″ may appear in both σ- and π-polarized orthoaxial spectra, whereas transitions of symmetry type E′ → E″ *or* E″ → E′ may appear in σ-polarized spectra but *not* in π-polarized spectra. According to these selection rules, the *degree-of-polarization* (P) quantity, defined in footnote *c* of Table III, may have any value between −1 and +1 for E′ → E′ and E″ → E″ transitions, but it is restricted to a value of −1 for E′ → E″ and E″ → E′ transitions. The P values shown in the last column of Table III indicate significant deviations from these selection rules, and it is clear that any classification of transitions (or states) according to C_4* symmetry properties must be considered highly approximate. However, as a first approximation in our energy-level analyses, it was useful to assign C_4* "parentage" labels to the transitions listed in Table III. These assignments were based on the relative signs and magnitudes of the P values observed within the various J-multiplet transition manifolds.

Within the C_4 symmetry approximation, the transition polarization data of Table III are most consistent with an E″ (C_4*) parentage label for the ground crystal-field level of $^4I_{15/2}$ and the following assignments for levels 27–53 (see Tables II and III for the energy-level numbering scheme): E′, levels 28, 29, 31, 33, 36, 37, 39, 40, 43, 45, 48, 49, 50, and 51; E″, levels 27, 30, 32, 34, 35, 38, 41, 42, 44, 46, 47, 52, and 53. Transition polarization data obtained from measurements at sample temperatures of 50 and 100 K suggest an E′ assignment for level 2 (at 85 cm^{-1}) and an E″ assignment for level 3 (at 118 cm^{-1}) of the $^4I_{15/2}$ (ground) multiplet. These energy-level assignments were used in our initial crystal-field calculations and analyses (based on a crystal-field Hamiltonian of C_4 symmetry—see eq 9 and related discussion). In these calculations, all 54 of the experimentally located energy levels (listed in Table II) were included in the parametric fits of calculated-to-empirical energy-level data, but only 30 of the levels (numbers 1–3 and 27–53) were constrained to be of a particular symmetry (E′ or E″ as specified above).

The calculated-to-empirical data fits obtained within the C_4 symmetry approximation (as described above) were generally unsatisfactory. The root-mean-square deviation between calculated and experimentally observed energies was a respectable 14.6 cm^{-1}, but the calculations could not reproduce the relative *ordering* of symmetry-assigned levels within several J-multiplet manifolds ($^2H_{11/2}$, $^4F_{7/2}$, and $^2G_{9/2}$). The crystal-field parameter values obtained from our C_4 symmetry-constrained calculations are shown in Table IV.

In a second series of calculations, we removed the C_4 symmetry constraints and incrementally added lower symmetry interaction terms to our phenomenological crystal-field Hamiltonian. In the final calculations of this series, the crystal-field Hamiltonian included the full complement of interaction terms required for C_2 crystal-field symmetry (within the one-electron approximation for crystal-field interactions), and this Hamiltonian contained 14 crystal-field parameters (9 *real* and 5 *imaginary*). These calculations produced data fits with a root-mean-square deviation of 9.9 cm^{-1} between calculated and experimentally observed energies, and the eigenvalues obtained from these calculations are listed in the third column of Table II. The crystal-field parameter values derived from the data fits are shown in the last column of Table IV. The eigenvectors of the C_2 crystal-field Hamiltonian show very strong C_4* parentage within the $^4S_{3/2}$ and $^4F_{3/2}$ multiplets (i.e., there is very little mixing between the $M_J = \pm^1/_2$, and $M_J = \pm^3/_2$ angular momentum components), but there is extensive mixing of C_4* symmetry components in the other multiplet manifolds. An M_J-component analysis is shown in Table V for the first three crystal-field levels of the $^4I_{15/2}$ (ground) multiplet.

The atomic Hamiltonian ($\hat{H}_a$) was parametrized by fitting the experimentally characterized baricenter energies listed in Table II (for 11 J-multiplet manifolds). The atomic parameter values

Table V. Major M_J Components Calculated for the First Three Crystal-Field Levels of the $^4I_{15/2}$ (Ground) Multiplet[a]

level no.	major M_J components of eigenvectors[b]
1	$\pm^3/_2$ (30%), $\pm^5/_2$ (28%), $\pm^1/_2$ (12%), $\pm^{11}/_2$ (10%), $\pm^{13}/_2$ (10%), $\pm^7/_2$ (6%), $\pm^9/_2$ (4%)
2	$\pm^7/_2$ (18%), $\pm^1/_2$ (17%), $\pm^{11}/_2$ (16%), $\pm^{13}/_2$ (15%), $\pm^5/_2$ (13%), $\pm^9/_2$ (8%), $\pm^{15}/_2$ (7%), $\pm^3/_2$ (6%)
3	$\pm^{13}/_2$ (22%), $\pm^{11}/_2$ (18%), $\pm^1/_2$ (18%), $\pm^7/_2$ (13%), $\pm^9/_2$ (9%), $\pm^{15}/_2$ (8%), $\pm^3/_2$ (7%), $\pm^5/_2$ (5%)

[a] Calculations based on the Hamiltonian parameters given in Table IV for C_2 symmetry. [b] Identified according to percent (%) contributions to the complete eigenvectors.

shown in Table IV yield a baricenter fit with a root-mean-square deviation of 5.1 cm^{-1}. These atomic parameters were used in both our *final* C_4 and *final* C_2 crystal-field calculations. The crystal-field calculations were started out at many different points in the B_{km} parameter space, and they generally converged reasonably rapidly to yield the B_{km} values listed in Table IV. However, our empirical data set of 54 levels is not sufficient to support a truly definitive C_2 analysis.

Discussion

The polarized optical absorption measurements and energy-level analyses performed in this study clearly demonstrate that the 4f-electron/crystal-field interactions in $Er(C_2O_4)(C_2O_4H)\cdot 3H_2O$ do not have the tetragonal symmetry of the macroscopic crystal structure. This may be attributed to local structural distortions and electronic perturbations caused by the bioxalate hydrogen atoms, which are disordered in the macroscopic crystal structure. The presence of these hydrogen atoms in the coordination spheres of the erbium ions requires that the *actual* Er^{3+} site symmetry be no higher than C_2. Our results indicate that the crystal-field energy-level structure of Er^{3+} in $Er(C_2O_4)(C_2O_4H)\cdot 3H_2O$ can be reasonably well accounted for by a crystal-field Hamiltonian of C_2 symmetry, but they do not rule out the possible importance of lower symmetry contributions to the crystal-field interactions. The results also show that the crystal-field states within multiplets of low J values ($J = {}^3/_2$ or ${}^5/_2$) retain strong C_4* symmetry character, whereas this is not the case for the majority of states derived from multiplets with $J > {}^5/_2$. According to our crystal-field energy-level calculations, the *ground* crystal-field level of $^4I_{15/2}$ has approximately 78% E'' (C_4* parentage) character. Eigenvectors calculated for levels 32 ($^4S_{3/2}$) and 47 ($^4F_{3/2}$) exhibit greater than 96% E'' ($M_J = \pm^3/_2$) character, and eigenvectors calculated for levels 33 ($^4S_{3/2}$) and 48 ($^4F_{3/2}$) exhibit greater than 96% E' ($M_J = \pm^1/_2$) character. The $^4I_{15/2} \rightarrow {}^4S_{3/2}$ and $^4I_{15/2} \rightarrow {}^4F_{3/2}$ transition polarization results shown in Table III reflect these eigenvector compositions.

The atomic Hamiltonian used to fit the $4f^{11}$ J-multiplet baricenter energies of Er^{3+} in $Er(C_2O_4)(C_2O_4H)\cdot 3H_2O$ has parameter values very similar to those reported for Er^{3+} in $ErCl_3\cdot 6H_2O$[9] and in $Na_3[Er(C_4H_4O_5)_3]\cdot 2NaClO_4\cdot 6H_2O$,[7] and the SL (term) compositions of the $|4f^{11}[SL]J\rangle$ state vectors are, therefore, similar to those shown in Table IV of ref 7. This present paper reports the *first* detailed optical measurements and energy-level analysis of any $Ln(C_2O_4)(C_2O_4H)\cdot 3H_2O$ system, so our crystal-field Hamiltonian and its parametrization cannot be compared with previous studies. However, we have recently carried out optical luminescence measurements on *microcrystalline* samples of $Eu(C_2O_4)(C_2O_4H)\cdot 3H_2O$ and Eu^{3+}-doped $Y(C_2O_4)(C_2O_4H)\cdot 3H_2O$,[10] and the unpolarized $^7F_J \leftarrow {}^5D_0$ emission spectra observed for these samples are entirely compatible with the crystal-field model adopted in the present study. Each $^7F_J \leftarrow {}^5D_0$ transition manifold is split into $2J + 1$ components, and the energy-level spacings within the $^7F_1$ multiplet manifold are close to those predicted by the rank-two crystal-field parameters of Table IV (C_2 symmetry). We have not yet succeeded in preparing single crystals of the europium compounds large enough for *polarized* absorption and emission measurements. The growth of good, optical-quality crystals is exceedingly slow.

Finally, we note that neither $Er(C_2O_4)(C_2O_4H)\cdot 3H_2O$ nor Er^{3+}-doped $Y(C_2O_4)(C_2O_4H)\cdot 3H_2O$ yields any detectable photoluminescence.[10] The ligands coordinated to the Er^{3+} ions are rich in high-frequency vibrational modes, and these modes provide efficient nonradiative relaxation pathways between the relatively closely spaced J-multiplet manifolds. In the erbium compounds, the largest energy gap between multiplets is *ca.* 6200 cm^{-1} (between $^4I_{15/2}$ and $^4I_{13/2}$), which is less than 2 vibrational quanta of the water molecule's stretching modes. This may be contrasted with the $^7F_6$–$^5D_0$ energy gap in the europium compounds, which is ca. 12 500 cm^{-1}.

Acknowledgment. This work was supported by the U.S. National Science Foundation (NSF Grant CHE-8820180 to F.S.R.). We also gratefully acknowledge help and advice from Dr. Michael F. Reid, and we thank Dr. Charles O'Conner (University of New Orleans) for providing the initial crystal sample used in this study.

(10) Schoene, K. A.; Metcalf, D. H.; Richardson, F. S. Unpublished results.

Contribution from the Department of Chemistry, Texas A&M University, College Station, Texas 77843

Closed-Shell Electronic Structures for Linear L_nMXML_n Dinuclear Transition-Metal Complexes

Zhenyang Lin and Michael B. Hall*

Received March 28, 1991

The unparametrized Fenske–Hall method is used to study the closed-shell electronic requirements for a large number of linear L_nMXML_n (n = 3–6) dinuclear transition-metal complexes. The linearity of the dinuclear complexes relates closely to the two 3-center π bonds in the M–X–M unit. The occupation of the corresponding π-antibonding orbitals results in a severely bent M–X–M geometry. Linear dinuclear complexes with vertex-sharing tetrahedra, L_3MXML_3, require a d^8–d^8 closed-shell configuration. For linear L_5MXML_5 complexes with a structure of vertex-sharing octahedra, a d^4–d^4 configuration will satisfy the closed-shell requirement. Complexes L_6MXML_6 with a linear vertex-sharing pentagonal-bipyramidal geometry correspond to a d^2–d^2 closed-shell configuration.

Introduction

The large number of L_nMXML_n (n = 3–6; X = main-group atom, generally group 14–16) dinuclear transition-metal complexes form a unique class of compounds in transition-metal chemistry.[1] The M–X–M bond angles are particularly interesting, because one should be able to correlate their geometry with the bonding

(1) Herrmann, W. A. *Angew. Chem., Int. Ed. Engl.* **1986**, *25*, 56.

0020-1669/91/1330-3817$02.50/0